Numerical study of heat transfer in a non-Newtonian Carreau-fluid between rotating concentric vertical cylinders

K. Khellaf, G. Lauriat[*]

Lavoisier Building, Université de Marne-la-Vallée, 77454 Marne-la-Vallée cedex 2, France

Abstract

Centrifugally forced convection, mixed and natural convection are numerically studied in a short vertical annulus with a heated and rotating inner cylinder. The cooled outer cylinder is at rest and the hortizontal endplates are assumed adiabatic. The effect of a non-Newtonian shear thinning viscosity modeled by the Carreau-shifted constitutive equation is examined. Computations were performed for different values of the flow index and Weissenberg number with the Prandtl number based on the zero-shear-rate viscosity, the radius ratio and the ratio of height to gap spacing are kept fixed. The results show that the shear thinning effect decreases the friction factor at the rotating cylinder and increases the heat transfer through the annular gap. It is also shown that the reduction in apparent viscosity may produce oscillatory flows, especially for centrifugally forced convection. © 2000 Elsevier Science B.V. All rights reserved.

1. Introduction

In this paper, we are concerned with the flow and heat transfer in the annular space between two concentric cylinders where the inner cylinder is rotated and the outer cylinder is at rest. At low enough speed of rotation, the flow between infinite concentric isothermal cylinders is one-dimensional and purely tangential. Analytical solutions of the momentum equation can be then readily obtained for non-Newtonian but viscous fluids.

There have been extensive works concerning the problem of hydrodynamic stability of isothermal flow in an annulus between rotating vertical cylinders and numerous studies have shown that the Couette flow of viscous fluid is unstable to axisymmetric disturbances when the rotational Reynolds number, or Taylor number, exceeds a certain critical value which is a function of the rheological property of the fluid, radius ratio and aspect ratio of the annular space. Amplifications of these

disturbances lead first to the transition to a laminar, two-dimensional cellular vortex flow in the r–z sections of the annulus, referred to as Taylor-vortex flow. Linear and non-linear aspects of the Taylor problem have been the subject of comprehensive reviews by DiPrima and Swinney [1] and, more recently, by Kataoka [2] for Newtonian fluids. As the rotation speed is further increased, the development and amplification of three dimensional disturbances in Taylor–Couette flows takes the form of wavy Taylor vortices in the circumferential direction which are established with traveling waves super-imposed on the Taylor vortex flow.

Practical applications of Taylor–Couette flow include catalytic chemical reactors [3], filtration devices [4], blood plasmaphoresis devices [5], plant cell bioreactors [6], ion exchangers [7], liquid-liquid extractors [8], and so on. Most of the fluids relevant to these processes are non-Newtonian and can be assumed viscous with an apparent viscosity depending on the shear rate. The stability criteria for non-Newtonian fluid models were considered in several works [9–14]. For example, in their experimental study on the stability of Couette flow of dilute polymer solutions, Rubin and Elata [12] predicted that the critical Taylor number increases with concentration while the associated wavelength remains constant. For a Bingham fluid, Nsom Eyenga and Cressely [13] showed that non-Newtonian behavior and plasticity have a stabilizing effect. Kouitat et al. [14] investigated theoretically and numerically the laminar Couette flow at the start-up stage of the fluid motion within a coaxial cylinder viscometer. Their results showed mainly that commonly used approximations for the flow shear rate are not appropriate unless restrictive experimental conditions are fulfilled.

For food and chemical processes, scraped surface heat exchangers are often employed to heat or to cool highly viscous fluids which exhibit non-Newtonian behavior [15]. In these applications, buoyancy effects are generally important due to the low speed of rotation used. Also, radial heating complicates both theoretical and experimental investigations. If the effects of a radial temperature gradient on the stability of Taylor–Couette flows has been the subject of considerable investigation for Newtonian fluids, the mutual interactions between buoyancy and rotational forces have not been adequately treated for non-Newtonian fluids in non-isothermal rotating systems. To the author's best knowledge, the study by Naimi et al. [16] is the one concerning convection heat transfer in non-Newtonian fluids. They performed a flow visualization study of the development and structure of Taylor–Couette vortices for the case of a power-law fluid (Carbopol 940) with and without axial flow in the forced convection regime. From their experimental study, they derived heat transfer correlations for various flow regimes.

The present study focuses attention on the non-Newtonian fluid motions and heat transfer in a Taylor apparatus of moderate aspect ratio filled with a fluid whose rheological behavior may be described by the shifted Carreau model (or modified power-law model). In comparison with the Newtonian case, this model involves four additional parameters, namely the zero- and infinite-shear-rate viscosities (μ_0 and μ_∞, respectively), the relaxation time of the fluid, λ, which describes the transition to a constant viscosity in the limit of zero shear rate, and the index of structure, n, which is a measure of the degree of non-Newtonian behavior. The numerical solutions reported here are for centrifugally forced convection, mixed and natural convection flow regimes. The effect of variations of the apparent viscosity of the fluid on instabilities, that are primarily centrifugal, are examined in detail.

2. Mathematical formulation

Consider a vertical Taylor reactor of finite length H' with the inner cylinder of radius r'_i rotating at constant angular velocity (and maintained at a given hot and uniform temperature T'_i. The outer cylinder
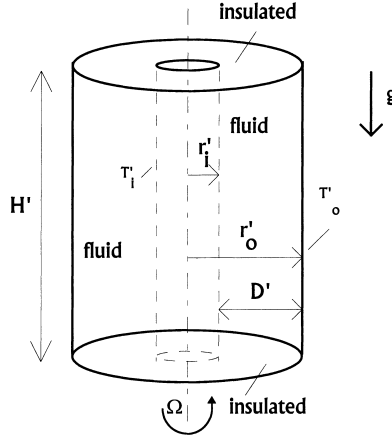
Fig. 1. Schematic view of the system.

of radius r'_o is at rest and isothermal at a cold temperature T'_o while the horizontal endwalls are assumed stationary and adiabatic (Fig. 1). The annulus gap is filled with a Boussinesq fluid, and the flow is assumed laminar, incompressible and axisymmetric. Due to the relatively low speed of rotation considered in the present study, the viscous heat generation is neglected in the energy equation. Non-Newtonian effects are considered for fluids obeying the Carreau constitutive relationship given by

$$\Gamma = \frac{\mu - \mu_\infty}{\mu_o - \mu_\infty} = (1 + \lambda^2 \dot{\gamma}^2)^{(n-1)/2} \tag{1}$$

where $\dot{\gamma}$ is the magnitude of the deformation rate tensor. In the following analysis, it is assumed that the parameters of this constitutive equation do not vary with temperature. For many concentrated polymer solutions and melts, it can be assumed that $\mu_\infty \ll \mu_o$ (Bird et al. [17]). Here, μ_∞ is taken to be zero and Γ is the dimensionless apparent viscosity. The fluid is Newtonian if n is equal to unity and the shear-thinning behavior becomes more significant as n becomes smaller. Contrary to the more commonly used power-law model which predicts an infinite viscosity at the limit of zero shear rate when $n < 1$, the Carreau model leads to a smooth transition to a constant viscosity at the limit of zero shear rate ($\Gamma = 1$).

In dimensionless form, the geometry is characterized by the radius ratio, $K = r'_o/r'_i$, and the aspect ratio, $A = H'/(r'_o - r'_i)$. Temperature, velocity and lengths are made dimensionless by using $(T'_i - T'_o)$, $\Omega r'_i$, and $D' = (r'_o - r'_i)$ as temperature difference, velocity and length scales, respectively. When writing the constitutive Eq. (1) in terms of the dimensionless magnitude of the deformation rate tensor, ϕ, the flow index and the Weissenberg number, W, describe the rheological property of the fluid. The dimensionless apparent viscosity is then given by the following constitutive equation:

$$\Gamma = (1 + W^2 \phi)^{(n-1)/2}, \tag{2}$$

where

$$\phi = 2\left(\frac{\partial U_r}{\partial r}\right)^2 + 2\left(\frac{\partial U_z}{\partial z}\right)^2 + 2\left(\eta \frac{U_r}{f}\right)^2 + \left(\frac{\partial U_\theta}{\partial z}\right)^2 + \left(\frac{\partial U_z}{\partial r} + \frac{\partial U_r}{\partial z}\right)^2 + \left(f \frac{\partial}{\partial r}\left(\frac{U_\theta}{f}\right)\right)^2.$$

$\eta = K - 1$ is the curvature parameter and $f = \eta r + 1$ a radial function.

The dimensionless governing equations written in conservative form are as follows:

Continuity equation:

$$\frac{\partial}{\partial r}(fU_r) + \frac{\partial}{\partial z}(fU_z) = 0 \tag{3}$$

Equations of motion:

$$\frac{DU_r}{Dt} - \eta U_\theta^2 = -f\frac{\partial P}{\partial r} + \frac{1}{Re}\left\{\frac{\partial}{\partial r}\left(2f\Gamma\frac{\partial U_r}{\partial r}\right) + \frac{\partial}{\partial z}\left(f\Gamma\frac{\partial U_r}{\partial z}\right) + \frac{\partial}{\partial z}\left(f\Gamma\frac{\partial U_z}{\partial r}\right) - 2\Gamma\eta^2\frac{U_r}{f}\right\}, \tag{4}$$

$$\frac{DU_\theta}{Dt} + \eta U_\theta U_r = \frac{1}{Re}\left\{\frac{\partial}{\partial r}\left(f\Gamma\frac{\partial U_\theta}{\partial r}\right) + \frac{\partial}{\partial z}\left(f\Gamma\frac{\partial U_\theta}{\partial z}\right) - \frac{\eta}{f}U_\theta\frac{\partial(f\Gamma)}{\partial r}\right\}, \tag{5}$$

$$\frac{DU_z}{Dt} = -f\frac{\partial P}{\partial z} + \frac{1}{Re}\left\{\frac{\partial}{\partial r}\left(f\Gamma\frac{\partial U_z}{\partial r}\right) + \frac{\partial}{\partial z}\left(2f\Gamma\frac{\partial U_z}{\partial z}\right) + \frac{\partial}{\partial z}\left(f\Gamma\frac{\partial U_r}{\partial z}\right)\right\} + f\frac{Gr}{Re^2}, \tag{6}$$

Energy equation:

$$\frac{DT}{Dt} = \frac{1}{Re\,Pr}\frac{\partial}{\partial r}\left(f\frac{\partial T}{\partial r}\right) + \frac{\partial}{\partial z}\left(f\frac{\partial T}{\partial z}\right), \tag{7}$$

where

$$\frac{D}{Dt} = \frac{\partial(f)}{\partial t} + \frac{\partial}{\partial r}(fU_r) + \frac{\partial}{\partial z}(fU_z).$$

In the above equations, the Reynolds number, Re, Grashof number, Gr, and Prandtl number, Pr, are based on the fluid viscosity at zero shear rate. The dimensionless boundary conditions for the problem under consideration are:

$$U_\theta = 1, \quad U_r = U_z = 0, \quad T = 0.5 \quad \text{at the inner cylinder} \quad r = \frac{1}{\eta - 1} \tag{8}$$

$$U_\theta = 0, \quad U_r = U_z = 0, \quad T = -0.5 \quad \text{at the outer cylinder} \quad r = \frac{\eta}{\eta - 1} \tag{9}$$

$$U_\theta = U_r = U_z = 0 \quad \text{and} \quad \frac{\partial T}{\partial z} = 0 \quad \text{at the horizontal endwalls } z = 0, A. \tag{10}$$

The local shear stress at the inner wall is defined as

$$\tau = -\rho\nu_0\left[\Gamma r'\frac{\partial}{\partial r'}\left(\frac{U_\theta}{r'}\right)\right]_i, \tag{11}$$

and the averaged shear stress over the annulus height is

$$\tau_m = \frac{1}{H'}\int_0^{H'} \tau\, dz' \tag{12}$$

From Eqs. (11) and (12), we can define an averaged friction factor as

$$C_f = \frac{\tau_m}{1/2\rho(\Omega r_i')^2} \tag{13}$$

or in dimensionless form:

$$\text{Re } C_f = \frac{2}{A} \int_0^A \left[\Gamma \left(\eta - \frac{\partial U_\theta}{\partial r} \right) \right] dz. \tag{14}$$

The local Nusselt number for this problem is defined as the ratio of the actual to the conduction heat transfer. i.e.

$$\text{Nu}_L(r,z) = \frac{q_{\text{actual}}}{q_{\text{cond}}}, \tag{15}$$

where

$$q_{\text{cond}} = \frac{2\pi kH(T_i' - T_o')}{\ln(K)}. \tag{16}$$

The mean Nusselt number is defined as the vertical line-average of the local Nusselt numbers since the flow and temperature fields are assumed to be independent of the angular coordinate. The average of $\text{Nu}(r,z)$ on a cylindrical surface of radius r leads to the following expression in terms of dimensionless variables

$$\text{Nu}(r) = \frac{\ln(\eta+1)}{\eta} f \int_0^A \left(\frac{U_r T}{\text{Re Pr}} - \frac{\partial T}{\partial r} \right) dz. \tag{17}$$

For adiabatic horizontal endwalls, the mean Nusselt number must be independent of the radial position at steady state, that is $\text{Nu}(r) = \text{Nu}$. This condition was used to check the accuracy of the numerical results. Obviously, $\text{Nu} = 1$ at the conduction regime ($\text{Gr} = \text{Re} = 0$).

3. Numerical method

The governing equations were solved in transient form. A control-volume formulation based on staggered grids [18] and approximations of second-order central differences were used for all of the space derivatives. The SIMPLER algorithm was applied for handling the pressure–velocity coupling. The time integration was performed using an alternating-directional implicit (ADI) splitting scheme, and the tridiagonal matrix algorithm was employed to solve the resulting systems of algebraic equations, except for the pressure correction equation which was solved by an iterative method (line-by-line scheme). On account of the expected flow structure, uniform grids were used for all of the computations discussed in the present paper. A systematic effort was made to ensure that the solutions are grid independent in time as well in space. Table 1 shows the effect of the grid resolution on the

Table 1
Effect of the grid size on (a) the friction coefficient (Re C_f), and (b) mean Nusselt number (Re = 100, Gr = 0, A = 1, K = 5, Pr = 5)

n	W	21 × 21	41 × 41	61 × 61	81 × 81	101 × 101
(a)						
1.0	/	35.76	41.02	43.76	45.60	46.95
	05	25.39	28.91	30.64	31.74	32.53
	10	24.00	27.32	28.93	29.97	30.71
0.9	15	23.22	26.43	27.99	28.99	29.70
	20	22.68	25.82	27.34	28.31	29.00
	05	18.00	20.47	21.63	22.34	22.83
	10	16.05	17.98	19.31	19.93	20.37
0.8	15	14.99	16.69	18.06	18.64	19.05
	20	13.96	15.84	17.22	17.78	18.16
(b)						
1.0	/	2.128	2.067	2.055	2.051	2.048
	05	2.243	2.160	2.144	2.138	2.136
	10	2.314	2.227	2.210	2.203	2.202
0.9	15	2.356	2.267	2.249	2.242	2.240
	20	2.351	2.294	2.277	2.269	2.266
	05	2.272	2.188	2.166	2.159	2.156
	10	2.355	2.281	2.231	2.249	2.245
0.8	15	2.396	2.291	2.269	2.301	2.297
	20	2.420	2.312	2.290	2.337	2.333

averaged friction factor and mean Nusselt number for various flow indexes and Weissenberg numbers. As it can be seen, the grid size has a larger influence on the friction factor than on the heat transfer rate. From this grid study, it was concluded that a 81 × 81 grid can be considered as a good compromise between accuracy and computational costs for most of the calculations discussed in the present paper.

The computer code was also validated by comparing the present solutions with results reported in the literature. For an infinite Taylor column filled with a Newtonian fluid, the critical Reynolds number for an isothermal flow induced by the rotation of the inner cylinder was shown to be in close agreement with the analytical solutions of Taylor [19] and Davey [20]. The critical values determined numerically through gradual increases in Re are reported in Table 2 for annuli of radius ratios K = 1.01 and K = 2. Fig. 2 shows the variation of the dimensionless group (Re πC_f) as a function of Re for an annulus of large radius ratio (K = 2). Beyond Re = 68, which is very close to the critical value predicted theoretically by Davey [20] (Re = 68.2), the group (Re πC_f) increases sharply. The maximum

Table 2
Comparisons of critical Reynolds numbers for small-gap and for wide-gap annulus of infinite height (isothermal flows)

	$K = 1.01$	$K = 2$
Present work	$411 \leq Re_c \leq 412$	$68 \leq Re_c \leq 69$
Literature	$Re_c = 413.2$ [18]	$Re_c = 68.2$ [19]
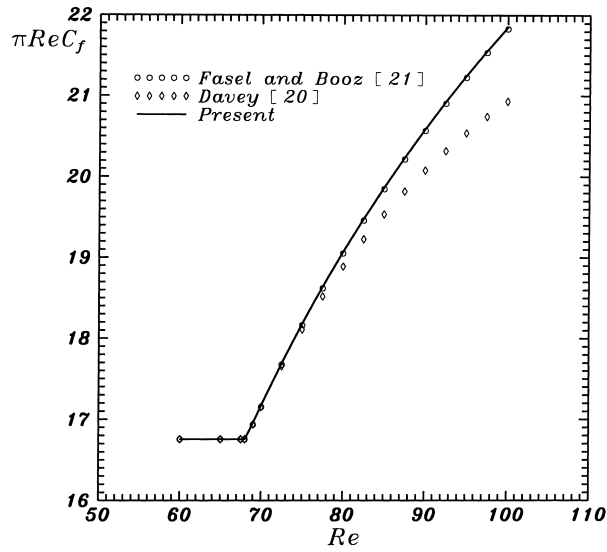
Fig. 2. Modified friction factor for an infinite, isothermal Taylor apparatus vs. Reynolds number ($K = 2$).
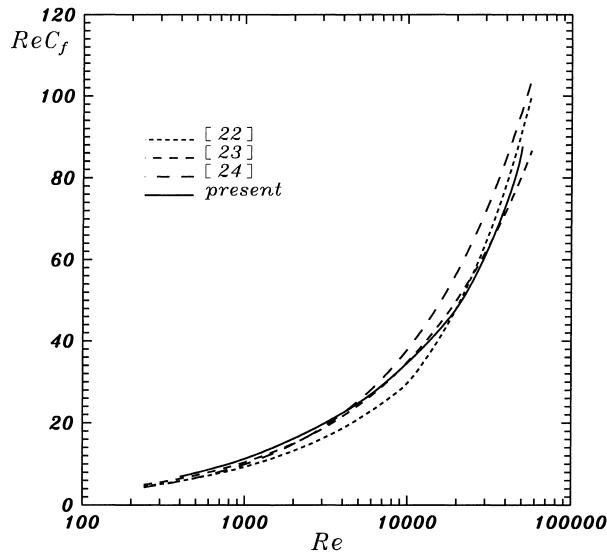
Fig. 3. Comparison of the computed friction factor with predictions of Wendt [22], Bjorklund and Kays [23] and Mizushina et al. [24] correlations ($K = 1.15$).

difference is less than 0.06% for Re $\leq$ 100 with the results of Fasel and Booz [21] while the discrepancies with the results of Davey [20] increase with Re and are about 4.2% at Re = 100.

Fig. 3 shows a comparison between the present results for the product Re C_f and the correlations from Wendt [22], Bjorklund and Kays [23], and Mizushina et al. [24] for $K = 1.15$ and Re varying

between 400 and 50,000. These correlations are expressed as Wendt [22]:

$$\mathrm{Re}\, C_\mathrm{f} = 0.460\,\mathrm{Re}^{0.5}(K^2 - K)^{0.25} \quad \text{for} \quad 400 \leq \mathrm{Re} \leq 10^4,$$

$$\mathrm{Re}\, C_\mathrm{f} = 0.073\,\mathrm{Re}^{0.7}(K^2 - K)^{0.25} \quad \text{for} \quad \mathrm{Re} \geq 10^4. \tag{18}$$

Bjorklund and Kays [23]:

$$\mathrm{Re}\, C_\mathrm{f} = 0.760\,\mathrm{Re}^{0.522}(K - 1)^{0.261}\left(\frac{K^2}{K + 1}\right) \text{for}\, 90 \leq \mathrm{Re}(K - 1) \leq 10^4. \tag{19}$$

Mizushina et al. [24]:

$$\mathrm{Re}\, C_\mathrm{f} = 0.512\,\mathrm{Re}^{0.580}(K - 1)^{0.29}\left(\frac{K^2}{K + 1}\right) \quad \text{for}\, 10^3 \leq \mathrm{Re}(K - 1) \leq 10^6. \tag{20}$$

The maximum relative differences between the present results and the $\mathrm{Re}\, C_\mathrm{f}$ values calculated from any of the above correlations was found to be less than 17%, the largest discrepancies occurring at $\mathrm{Re} \leq 1000$ with the correlation of Wendt [22].

The computations of the friction factor were also compared with the measurements of Cognet [25] who reported data for the local friction factor at mid-height of a Taylor cell for a radius ratio $K = 1.1$ and $160.9 \leq \mathrm{Re} \leq 1206.7$. It was assumed in [25] that this local C_f may be considered as representative of the mean value. The results reported in Table 3 show first that this assumption is well supported by the present computations in the low range of Re while its validity becomes questionable when increasing Re. Secondly, it is seen that the maximum relative difference between the measurements and the computations is mostly less than 10%.

Table 3
Comparisons of local values of the friction coefficient, $(\mathrm{Re}\, C_\mathrm{f})^*$, with experimental data from Cognet [25], relative differences and averaged value of $\mathrm{Re}\, C_\mathrm{f}$ over the height of a Taylor cell (isothermal flows)

Re	$(\mathrm{Re}\, C_\mathrm{f})^*$ [25]	$(\mathrm{Re}\, C_\mathrm{f})^*$	$\varepsilon(\%)$	$\mathrm{Re}\, C_\mathrm{f}$
160.96	3.015	3.119	3.3	3.083
175.51	3.236	3.522	8.1	3.446
206.18	3.757	4.180	10.1	4.052
249.19	4.504	4.832	6.8	4.690
294.41	5.000	5.337	6.3	5.220
350.70	5.495	5.839	5.9	5.778
413.31	5.949	6.314	5.8	6.330
479.09	6.285	6.759	7.0	6.861
564.15	6.579	7.279	9.6	7.497
641.31	6.918	7.710	10.3	8.033
717.84	7.168	8.106	11.6	8.532
810.49	7.384	8.551	13.6	9.101
899.04	7.863	8.946	12.1	9.612
983.47	8.530	9.300	8.3	10.040
1098.26	9.045	9.749	7.2	10.669
1206.73	9.762	10.147	3.8	11.200

Table 4
Comparisons of the minimum and maximum values of the stream-function for different Reynolds numbers ($A = 1$, $K = 2$, $\text{Pr} = 13$, $\text{Gr} = 769$)

Re	Re $\psi_{\min}$	Re $\psi_{\min}$ [24]	Re $\psi_{\max}$	Re $\psi_{\max}$ [24]
10	0	-1.3×10^{-5}	0.58	0.61
50	-0.050	-0.049	0.70	0.71
100	-0.84	-0.82	1.76	1.60

When increasing the Reynolds number for annuli of finite height, $A = 3.8$ and $A = 5.2$, closed with solid endwalls, the 4-2-4 and 4-6-4 cell transitions were recovered at almost the same critical Reynolds numbers than those reported by Ball and Farouk [26].

Table 4 shows a comparison of the minimum and maximum values of the stream-function obtained in the present work with the value given by Ho and Tu [27] for different Reynolds numbers. Here, the inner rotating vertical cylinder is heated while the outer one is cooled and at rest. The horizontal endwalls are stationary and insulated. The results reported in Table 3 are for dominant natural convection ($\text{Re} = 10$), mixed convection ($\text{Re} = 50$), and dominant forced convection ($\text{Re} = 100$). It should be noted that the computations were carried out by using the same uniform mesh as in Ho and Tu [27] (41×41 grid). A fairly good agreement between the present results and those of Ho and Tu [27] can be seen, except for the very weak secondary cell at $\text{Re} = 10$ which was not found without increasing the grid resolution.

4. Results and discussion

In order to focus attention on the flow, thermal and non-Newtonian parameters, the geometry of the annulus is fixed at $A = 1$ and $K = 5$, and the Prandtl number at $\text{Pr} = 5$ throughout the present study. The value of the Prandtl number may vary in a large range for non-Newtonian fluids, especially for polymeric liquids. However, the effect of Pr on temperature distribution for cavity flows is generally small as Pr is greater than unity. Therefore, we kept Pr fixed at a value which corresponds to dilute solutions of polymer in water.

4.1. Effects of the flow index

Figs. 4 and 5 display the variations of the mean Nusselt number as a function of the flow index for various Reynolds and Grashof numbers, and for two Weissenberg numbers ($W = 10$ and 100, respectively). A strong Nu-dependence with n is evidenced according to the flow regime. As n tends towards unity, the solutions merge with the Newtonian ones, whatever W is. Therefore, the effect of the Weissenberg number is larger at low value of the flow index.

At very low speed of rotation of the inner cylinder ($\text{Re} = 1$), natural convection dominates at $\text{Gr} = 2000$. Figs. 4 and 5 show that the Nusselt number decreases with increasing the flow index from $n = 0.6$ to 1, the minimum value being obtained for a Newtonian fluid ($n = 1$) both for $W = 10$ and $W = 100$. To assume (independent of n can be considered as a first approximation so that we obtain

$$\frac{\partial \Gamma}{\partial n} = 0.5\Gamma[\ln(1 + W^2 \phi)] \tag{21}$$
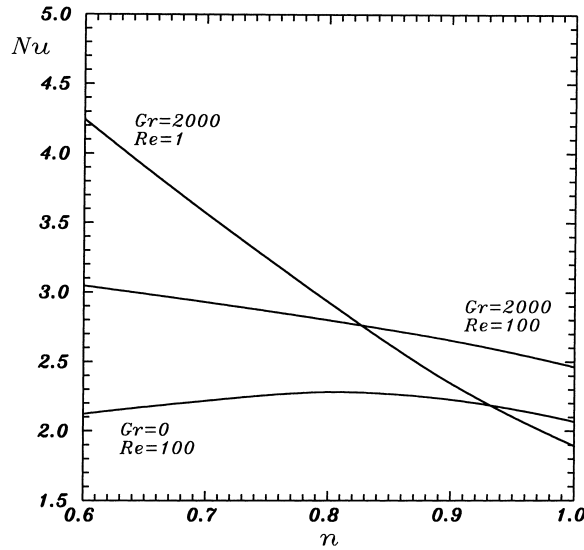
Fig. 4. Average Nusselt number vs. flow index for $W = 10$ ($A = 1$, $K = 5$, $\mathrm{Pr} = 5$).
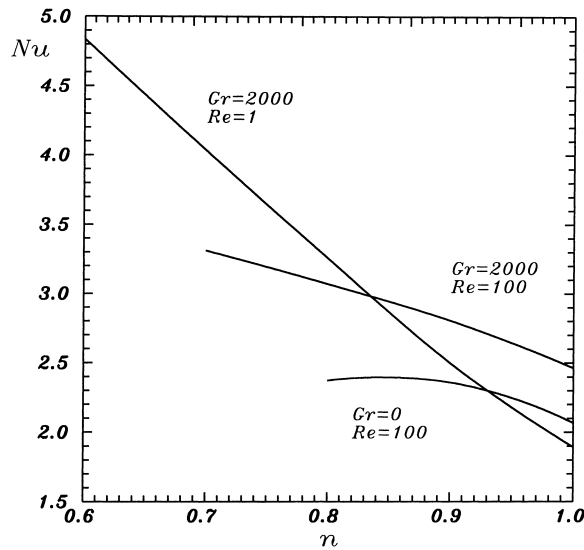
Fig. 5. Average Nusselt number vs. flow index for $W = 100$ ($A = 1$, $K = 5$, $\mathrm{Pr} = 5$).

Since the Γ-derivative with respect to n is always positive, Γ and thus the apparent viscosity increase with the flow index. Therefore, the flow rate increases as n is reduced. In turn, Nu increases. Also, the slope of the Nu-curves is more important for $W = 100$ than for $W = 10$ since Eq. (21) shows that $\partial \Gamma / \partial n$ increases with W.

For forced convection (Re $= 100$ and Gr $= 0$), the variations of Nu shown in Fig. 4 and Fig. 5 exhibits only modest variations in magnitude in the range $0.6 \leq n \leq 1$ for $W = 10$. At $W = 100$, it was not possible to pursue the calculations for n below 0.8 approximately because the flow field was found

becoming chaotic as it will be discussed later. The assumption of (independent of n does not hold at $n = 0.8$ due to the high shear rate produced by rotation. Therefore, Eq. (21) is not appropriate to predict the flow behavior at low flow index for centrifugally forced convection. However, inspection of Eq. (2) shows that the fluid viscosity is small since ϕ is large and $n \leq 1$. This explains the relative insensitivity of heat transfer to the flow index because non-Newtonian effects are less important for low apparent viscosity.

In the mixed convection regime (Re $= 100$ and Gr $= 2000$), rotation decreases the apparent viscosity and thus amplifies the action of the buoyancy force at n values close to unity ($0.85 \leq n \leq 1$). Further decreases in flow index result in a rapid change in the flow structure: the angular velocity component dominates over both radial- and vertical velocity components so that the mass flow transferred from the hot inner cylinder to the cold outer cylinder is reduced. Consequently, the Nu values for mixed convection lie between those found for natural convection and those for forced convection. At $W = 100$, the action of buoyancy force damps the oscillatory behavior and the steady-state solution is extended down to $n \cong 0.7$. Fig. 4 Fig. 5 show that there exists a critical flow index, defined by the intersection of natural and mixed convection curves, beyond which rotation enhances heat transfer. Obviously, this critical value decreases when increasing Gr.

Fig. 6 shows the streamlines and isotherms at $W = 100$ for natural and forced convection flows. Fig. 6(a) and (b) exemplifies the streamline patterns (LHS) and isotherm distributions (RHS) for natural convection with Gr $= 2000$. At the highest value of the flow index considered ($n = 0.9$), the flow adjacent to the inner cylinder consists of a layer of heated fluid moving upward and having a structure qualitatively similar to that is found within an annulus filled with a Newtonian fluid, featuring a clockwise recirculating motion. Furthermore, there exists a thermal boundary layer along the inner cylinder. When decreasing the apparent viscosity by changing n to 0.6 (Fig. 6b), the isotherms tend to become more stratified at the upper part of the annulus and the thermal boundary layer along the inner
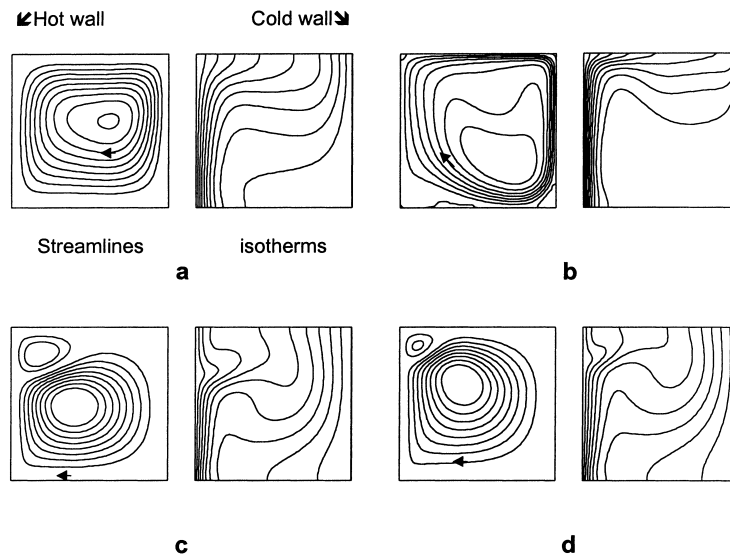
Fig. 6. Isotherms (T: $-0.5(0.1)0.5$) and streamlines at $W = 100$ ($A = 1$, $K = 5$, Pr $= 5$). (a) $n = 0.9$, Re $= 1$, Gr $= 2000$, ψ: $-18(2)0$; (b) $n = 0.6$, Re $= 1$, Gr $= 2000$, ψ: $-35(5)0$; (c) $n = 0.9$, Re $= 100$, Gr $= 0$, ψ: $-0.04(0.005)0.01$; (d) $n = 0.8$, Re $= 100$, Gr $= 0$, ψ: $-0.04(0.005)0.01$.

cylinder becomes thinner. A large portion of the fluid appears to be almost isothermal at a temperature close to that of the outer cylinder. In addition to the intensified recirculating flow, the streamlines feature a thin buoyancy-driven boundary layer along the outer cylinder. The flow and heat transfer rate are approximately increased twice. Heat is mainly transferred by conduction at the inner cylinder while convective effects predominate at the outer cylinder. In the forced convection regime (Re = 100 and Gr = 0), one may observe in Fig. 6(c) a pair of counter-rotating cells. For $n = 1$, the flow pattern was found to consist of two stationary cells, symmetric to a horizontal plane through the annulus mid-height since the present results are for a Taylor apparatus of aspect ratio $A = 1$. When decreasing the flow index, the two-cell flow structure persists at first but the lower clockwise cell can be seen to grow and intensify progressively while the upper counterclockwise recirculating flow becomes substantially impeded for $n = 0.9$ (Fig. 6(c)). The isotherms show distorted shapes corresponding to the convection field in the vicinity of the recirculating flow structures. For $n = 0.8$, there is only a pocket of recirculating flow close to the rotating inner cylinder and near its top (Fig. 5(d)). The changes in Nusselt numbers for these two flow indexes are small.

For a Newtonian fluid, the numerical results obtained in this paper are in close agreement with those of Cliffe [28], especially for the value of the critical Reynolds number at which a Hopf bifurcation to unstable flows occurs (Re $\cong$ 150 for $A = 1$). When the flow index decreases, the apparent fluid viscosity becomes very small, even at moderate shear rates. Therefore, the onset of flow instabilities occurs at lower Reynolds numbers than for a Newtonian fluid. For example, at $n = 0.7$ an unsteady but periodical flow regime is established for Re = 100 and $W = 50$. The numerical solutions discussed in what follows where performed on a 101×101 uniform grid. The time evolution of the velocity components at the middle of the square section of the annular space ($r = z = 0.5$) are shown in Fig. 7 for large enough dimensionless time of integration ($t \geq 1800$) at which a periodic asymptotic state is reached. It should be noted here that such a flow behavior is purely centrifugal since the buoyancy effects are assumed to be negligible. In order to show the periodical nature of the asymptotic flow
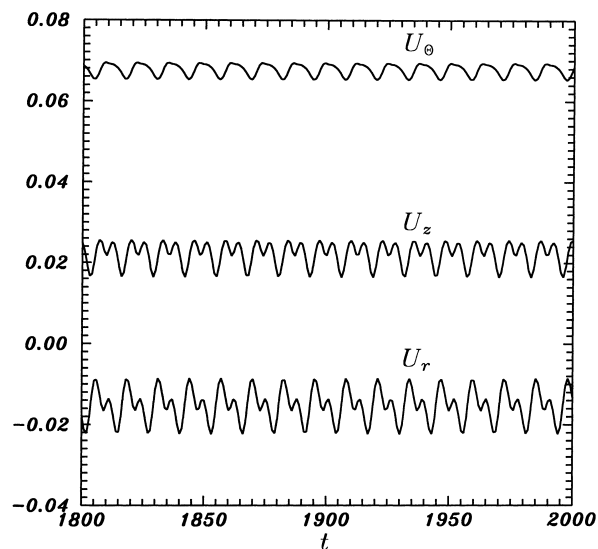
Fig. 7. Time evolution of the velocity components at the middle of the annulus section for the periodic regime at Re = 100, Gr = 0, $n = 0.7$ and $W = 50$ ($A = 1$, $K = 5$, Pr = 5).
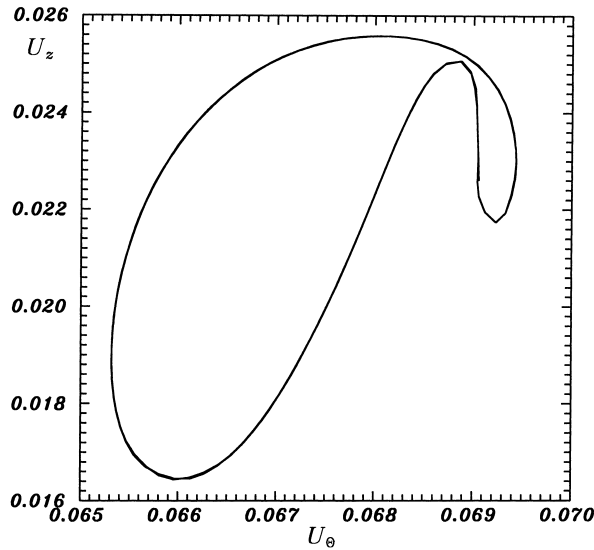
Fig. 8. Phase portrait for Re = 100, Gr = 0, $n = 0.7$ and $W = 50$ ($A = 1$, $K = 5$, Pr = 5).

regime, a phase portrait of (U_z, U_θ) built at mid-point is plotted in Fig. 8. The data shown in Fig. 8 are for every time step during the time interval $1800 < t < 3200$ with 12,820 iterations per cycle. A limit cycle representing more than 100 periods was then obtained without any dispersion. This result illustrates the precisely periodic nature of the asymptotic flow.

The streamlines are shown for $n = 0.7$ and $W = 50$ in Fig. 9 over one oscillation period for six snapshots equally spaced. It can be seen that the flow instabilities are basically caused by perturbations arising along the inner rotating cylinder where the shear rate is the highest. These instabilities take the form of little counter-rotating cells at the upper part of the wall which move up and down and amplify downward. At the end of the period, the strongest secondary cell is confined at the bottom corner of the cavity. At the point M ($r = 0.075$, $z = 0.5$), the oscillations have a frequency $f_1 = 0.078 \pm 0.002$ (corresponding to a period of $\Delta t = 12.82$). This result may lead to a possible three-dimensional perturbation which can induce a fully three-dimensional flow.

| t_0 | $t_0 + \Delta t/5$ | $t_0 + 2\Delta t/5$ | $t_0 + 3\Delta t/5$ | $t_0 + 4\Delta t/5$ | $t_0 + \Delta t$ |
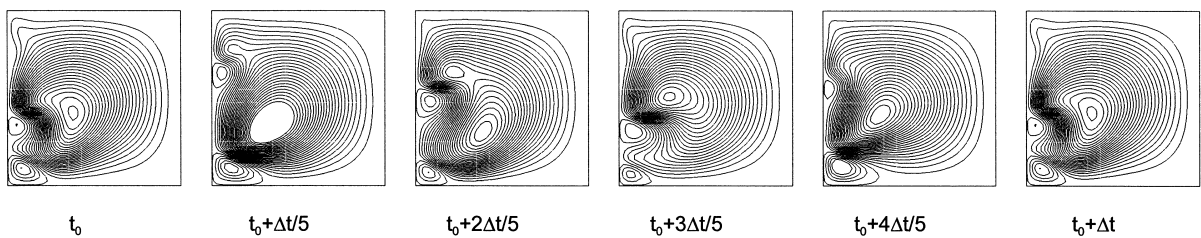
Evolution of the stream-function for established regime.

ψ : -0.008(0.002)0.048, Re = 100, Ra = 0, n = 0.7, W = 50, t_0 = 1000 and $\Delta t \cong$ 12,82

Fig. 9. Streamlines at six equally spaced times over one period ($t_0 = 1000$ and $\Delta t = 12.82$). ψ: $-0.008(0.002)0.048$, Re = 100, Gr = 0, $n = 0.7$, $W = 50$ ($A = 1$, $K = 5$, Pr = 5).

For Re = 100, the value of the flow index at which the flow becomes unsteady (Fig. 5) is located between $n = 0.75$ and $n = 0.8$. When the gravity effects are taken into account, this critical n value is decreased. For example, it has been found to be in the range [0.65, 0.7] at Gr = 2000. Therefore, buoyancy forces have a stabilizing effect. For pure natural convection flows, all the cases investigated in the present study were found steady at Gr = 2000. The onset of flow instabilities started to appear at flow indexes less than $n = 0.6$.

4.2. Effects of the weissenberg number

For a given flow index and constant shear rate, the derivative of the apparent viscosity with respect to W reads:

$$\frac{\partial \Gamma}{\partial W} = (n - 1)W[1 + W^2\phi]^{(n-3)/2} \tag{22}$$

Thus, the apparent viscosity decreases when increasing the Weissenberg number since $n \leq 1$, and the flow rate increases with W. The non-Newtonian shear thinning behavior is evidenced from Fig. 10 where the averaged friction factor at the inner wall is plotted for various flow indexes as a function of W for centrifugally forced convection (Re = 100, Gr = 0).

Fig. 10 shows that the friction factor decreases (and thus the torque) as W increases. Obviously, the shear rate dependence of the viscosity is the highest at the rotating inner cylinder where the thickness of the boundary layer decreases when increasing W or decreasing n. When the flow index is reduced and W increased, the low value of the apparent viscosity first leads to multicellular flows, with a secondary cell adjacent to the rotating cylinder, and then to oscillatory flows. At the lowest values of the flow index considered in the present study, the flow was found becoming oscillatory for a Weissenberg number close to $W = 25$ at $n = 0.75$ and $W = 13$ at $n = 0.70$. Fig. 10 shows also that the influence of the Weissenberg number decreases as W increases. For $n \geq 0.8$, the friction factor at the inner cylinder
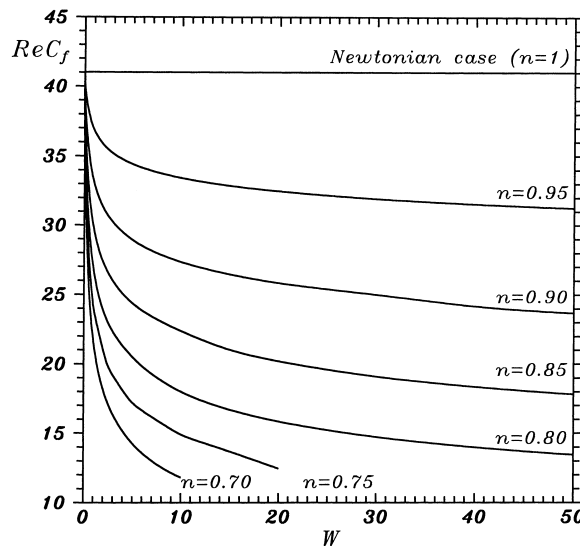
Fig. 10. Average friction coefficient at the inner cylinder versus Weissenberg number for various flow indexes.
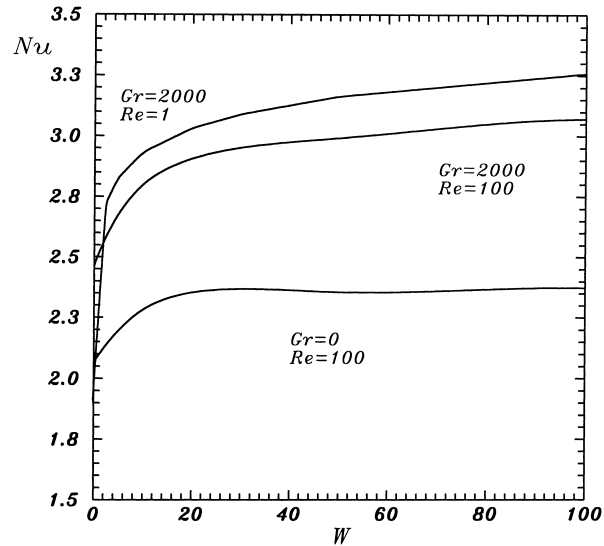
Fig. 11. Mean Nusselt number versus Weissenberg number for $n = 0.8$.

reaches an asymptotic value for W to about 100. This trend is to be expected from the constitutive Eq. (2) which shows that the shifted Carreau model turns into the power-law model as W increases. This W-independence of the apparent viscosity can also be explained by the asymptotic behavior of the W-derivative of Γ at large values of W. By assuming $W^2\phi \gg 1$, Eq. (22) becomes of the form

$$\frac{\partial \Gamma}{\partial W} \cong (n-1)W^{n-2}\phi^{(n-1)/2} \tag{23}$$

Therefore, $\partial\Gamma/\partial W$ tends towards 0 when increasing W since both exponents are negative. The apparent viscosity becoming constant, the velocity field are thus independent of W. However, it should be mentioned that the W-value at which the power-law limiting viscosity is reached depends also on the speed of rotation, through the dissipation function. It can thus be concluded that the domain of validity of the shifted Carreau model reduces as Re increases.

Fig. 11 presents the average Nusselt number versus the Weissenberg number for $n = 0.8$ and for the three flow regimes. Similar results were obtained for various values of the flow index. The Nu-curves exhibit a rapid increase at low Weissenberg numbers while the influence of W becomes less pronounced for $W \geq 20$, especially for centrifugally forced convection. Further increases in the Weissenberg number have almost no effect on heat transfer.

5. Conclusions

A numerical study of fluid flow and heat transfer has been conducted for non-Newtonian fluids confined in a vertical, differentially heated Taylor apparatus of aspect ratio $A = 1$ with rotating inner cylinder. Temperature dependent viscosity and viscous heating were neglected. The constitutive equation of the fluid is based on the shifted Carreau model. Three flow régimes were considered

according to the speed of rotation of the inner cylinder: centrifugally forced convection, mixed and natural convection. The calculations presented show that the shear thinning effects decrease the friction factor at the rotating cylinder and enhance the heat transfer rate through the annular gap, whatever the flow regime is. A parametric study of the effect of the flow index and Weissenberg number was conducted. The results indicate that the flow becomes oscillatory when decreasing the flow index or increasing the Weissenberg number, especially for centrifugally forced convection. Time evolutions of field variables are presented to describe this flow behavior.

6. List of symbols

A	aspect ratio $(H'/(r_o' - r_i'))$
C_f	averaged friction factor at the rotating inner cylinder Eq. (13)
D'	annular gap width $(r_o' - r_i')$
f	radial function $(f = \eta r + 1)$
g	gravitational acceleration
Gr	Grashof number $(g\beta(T_i' - T_o')D'^3/\nu_0^2)$
H'	column height
K	radius ratio (r_o'/r_i')
k	thermal conductivity
n	flow index or index structure
Nu_L	local Nusselt number Eq. (15)
Nu	mean Nusselt number Eq. (17)
Pr	Prandtl number based on the zero-shear-rate viscosity $\nu_0/\alpha)$
r'	radial coordinate
r	dimensionless radial coordinate $((r' - r_i')/D')$
r_i'	inner cylinder radius
r_o'	outer cylinder radius
Re	Reynolds number $(\Omega r_i'D'/\nu_0)$
t'	time
t	dimensionless time $(\Omega r_i't'/D')$
T	dimensionless difference temperature, $T = (T' - T_r')/(T_i' - T_o')$
T_i'	inner cylinder temperature
T_o'	outer cylinder temperature
T_r'	reference temperature, $T_r' = /(T_i' + T_o')/2$
U_r, U_z, U_θ	radial, axial and circumferential dimensionless velocity components
W	Weissenberg number $(\Omega r_i'\lambda/D')$
z'	axial coordinate
z	axial dimensionless coordinate (z'/D')

Greek symbols

α	thermal diffusivity
β	volumetric dilatation coefficient

η	curvature parameter ($\eta = K - 1$)
ϕ	dimensionless dissipation function
Γ	dimensionless viscosity ($\Gamma = \nu/\nu_0$)
λ	time relaxation parameter
μ	apparent dynamic viscosity
μ_0	zero-shear-rate dynamic viscosity
ν	apparent kinematic viscosity
ν_0	zero-shear-rate kinematic viscosity
Ω	angular velocity of inner cylinder
ψ	dimensionless stream function ($\partial\psi/\partial z = f(r)U_{\mathrm{r}}$)
θ	circumferential coordinate

References

[1] R.C. DiPrima, H.L. Swinney, in: H.L. Swinney, J.P. Gollub (Eds.), Hydrodynamic Instabilities and the Transition to Turbulence, Springer, Berlin, 1981, pp. 139–180.
[2] K. Kataoka, in: N.P. Cheremisinoff (Ed.), Encyclopedia of Fluid Mechanics, vol. 1, Gulf Publications, Houston, 1986, pp. 236–274.
[3] S. Cohen, D. Moalem Maron, Chem. Ing. J. 27 (1983) 87.
[4] U.B. Holeschovsky, C.L. Cooney, AICHE J. 37 (1991) 1219.
[5] G. Beaudoin, M.Y. Jaffrin, Artif. Organs 13 (1989) 43.
[6] D.A. Janes, N.H. Thomas, J.A. Callow, Biotech. Tech. 1 (1987) 257.
[7] J. Olin, W.W. Koenig, A.L. Babb, J.L. Mc Carthy, AICHE Symp. Ser. 50 (1954) 103.
[8] M.W. Davis, E.J. Weber, Ind. Eng. Chem. 52 (1960) 929.
[9] R.H. Thomas, K. Walters, J. Fluid Mech. 18 (1964) 33.
[10] S.K. Datta, Phys. Fluids 7 (1964) 1915.
[11] Y.L. Joo, E.S.G. Shaqfeh, Phys. Fluids 4 (1992) 2415.
[12] H. Rubin, C. Elata, Phys. Fluids 9 (1966) 1929.
[13] B. Nsom Eyenga, R. Cressely, Les cahiers de Rhéologie 8 (1989) 35.
[14] R. Kouitat, G. Maurice, M. Lucius, Les cahiers de Rhéologie 8 (1989) 17.
[15] C. Nouar, R. Devienne, M. Lebouché, J. Heat Transfer 3 (1986) 951.
[16] M. Naimi, R. Devienne, M. Lebouché, Int. J. Heat Mass Transfer 33 (1990) 338.
[17] R.B. Bird, R.C. Armstrong, O. Hassager, Dynamics of Polymeric Liquids, vol. I, Fluid Dynamics, Wiley, 1977.
[18] S.V. Patankar, Numerical Heat Transfer and Fluid Flow, Computational Methods in Mechanics And Thermal Sciences Series, McGraw Hill, New York, 1980.
[19] G.I. Taylor, Phil. Trans. R. Soc. London A 223 (1923) 289.
[20] A. Davey, J. Fluid Mech. 14 (1962) 336.
[21] H. Fasel, O. Booz, J. Fluid Mech. 138 (1984) 21.
[22] F. Wendt, Ingen. Arch. 4 (1933) 577.
[23] I.S. Bjorklund, W.M. Kays, J. Heat Transfer (Trans. ASME) 81 (1959) 175.
[24] T. Mizushina, R. Ito, T. Nakagawa, K. Kataoka, S. Yokoyama, Kogaku-Kogaku, Chem. Eng. Japan, (1976) 31.
[25] G. Cognet, Contribution à l'étude de l'écoulement de Couette par la méthode polarographique, thèse de doctorat, Université de Nancy, 1968.
[26] K.S. Ball, B. Farouk, J. Fluid Mech. 197 (1988) 479.
[27] C.J. Ho, F.J. Tu, Trans. ASME 114 (1992) 418.
[28] K.A. Cliffe, J. Fluid Mech. 135 (1983) 219.